

Atomic data for astrophysics: Ni XI^{*}

G. Del Zanna¹, P. J. Storey², and N. R. Badnell³

¹ DAMTP, Centre for Mathematical Sciences, Wilberforce Road, Cambridge, CB3 0WA, UK
e-mail: g.del-zanna@damtp.cam.ac.uk

² Department of Physics and Astronomy, University College London, Gower Street, London, WC1E 6BT, UK

³ Department of Physics, University of Strathclyde, Glasgow, G4 0NG, UK

Received 17 March 2014 / Accepted 30 April 2014

ABSTRACT

We present a new large-scale R-matrix scattering calculation for electron collisional excitation of Ni XI, carried out with the intermediate-coupling frame transformation method. The target includes all the main configurations up to $n = 4$, and is a significant improvement over earlier R-matrix (only three $n = 3$ configurations) and distorted-wave (DW) calculations. We find significant enhancements in the collision strengths of many of the strong transitions to the $n = 3, 4$ levels. They are due to the resonances that arise within the present large-scale target. This results in significant increases in the predicted intensities of the UV and visible forbidden lines within the $3s^23p^53d$ configuration, the strong EUV lines that result from the decays of the $3s^23p^53d$ levels to the ground state, and the decays from the $n = 4$ levels, which are visible in the soft X-rays. We find good agreement between predicted and observed line intensities in the EUV. With the present atomic data, lines from Ni XI can reliably be used for plasma diagnostics. We also revise some level energies and suggest a few new possible identifications.

Key words. atomic data – line: identification – Sun: corona – techniques: spectroscopic

1. Introduction

The resonance transition of Ni XI at 148.4 Å is one of the strongest lines in the extreme ultraviolet (EUV) region of the spectrum (see, e.g. Behring et al. 1972). This ion also produces several transitions in the soft X-rays and EUV. Ni XI lines are also observed in laboratory plasmas, such as those of the JET tokamak described by Mattioli et al. (2004).

Ni XI is isoelectronic with Fe IX, and lines from this ion are in principle useful to measure electron densities and temperatures. In particular, the two Ni XI lines at 207.9 and 211.4 Å are analogues of the Fe IX 241.7, 244.9 Å lines, which are an excellent density diagnostic (Storey et al. 2002), and are observed by the Hinode EUV Imaging Spectrometer (EIS, see Culhane et al. 2007), as discussed by Landi & Young (2009).

To date, the best scattering calculations for this ion are those of Aggarwal & Keenan (2007) and Bhatia & Landi (2011). Aggarwal & Keenan (2007) carried out, with the Dirac Atomic R-matrix Code (DARC, originally written by Norrington and Grant), R-matrix calculations involving the energetically lowest 17 levels, from the $3s^23p^6$, $3s^23p^53d$, and $3s3p^63d$ configurations. Bhatia & Landi (2011) carried out a scattering calculation with an extended target, including the main $n = 3, 4$ configurations. However, they used the distorted-wave (DW) approximation within the Flexible Atomic Code (FAC, see Gu 2004).

Both calculations have considerable limitations. As pointed out by Bhatia & Landi (2011), the small target employed by Aggarwal & Keenan (2007) limited the accuracy of their results. That an R-matrix calculation with a larger target was needed,

to include all the main resonances, was already pointed out by Aggarwal & Keenan (2007) themselves. Indeed, our earlier calculations for Fe IX (Storey et al. 2002) have clearly shown the need for a larger $n = 3$ target, to include all the main resonances contributing to the lowest three configurations, for ions of this sequence.

The DW calculations are inherently limited because the resonance enhancements are normally not included, and as a result collision strengths of the lowest configurations can easily be underestimated. Until recently, it was commonly thought that DW calculations were quite accurate for the higher configurations and this is often the case. However, there are many instances within an ion where DW calculations underestimate collision strengths by factors of two or more. For example, in O'Dwyer et al. (2012) we pointed out that collision strengths to the Fe IX $3s^23p^54s$ levels can be significantly underestimated if the resonances due to the $3s^23p^54p$ levels are not included. The effect is notable for the $3s^23p^54s$ levels because they have small collision strengths from the ground configuration. However, similar issues have been found for other Fe IX configurations in our recent large-scale R-matrix calculation (Del Zanna et al. 2014), but also in general with all other coronal iron ions: Fe X (Del Zanna et al. 2012b), Fe XI (Del Zanna & Storey 2013), Fe XII (Del Zanna et al. 2012a), and Fe XIII (Del Zanna & Storey 2013).

A new R-matrix calculation for all the main $n = 3, 4$ levels of Ni XI was therefore needed. The paper is organised as follows. In Sect. 2 we outline the methods we adopted for the scattering calculations. In Sect. 3 we present our results and in Sect. 4 we reach our conclusions.

2. Methods

The atomic structure calculations were carried out using the AUTOSTRUCTURE program (Badnell 2011) which originated

* The full dataset (energies, transition probabilities and rates) are only available in electronic form at our APAP website (www.apap-network.org) as well as at the CDS via anonymous ftp to cdsarc.u-strasbg.fr (130.79.128.5) or via <http://cdsarc.u-strasbg.fr/viz-bin/qcat?J/A+A/566/A123>

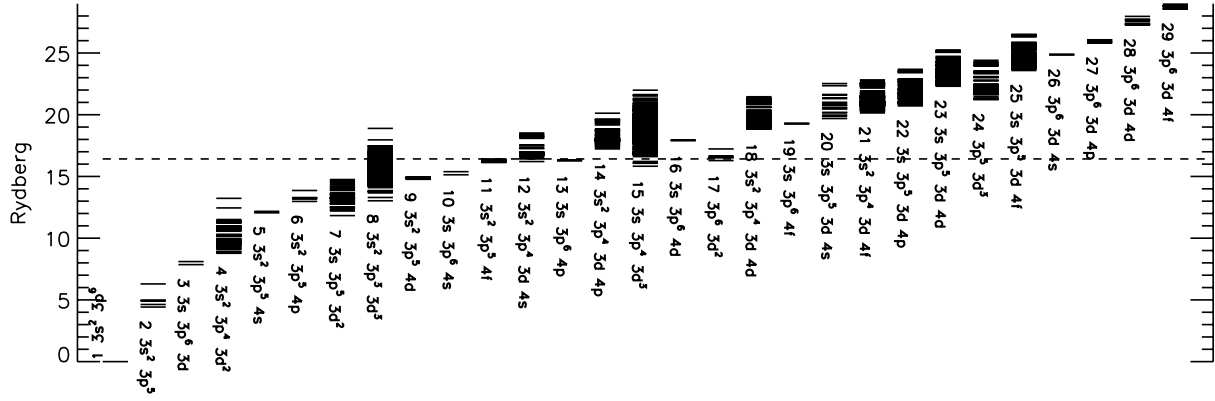


Fig. 1. *LS* terms of the target configuration basis. The lowest 273 terms which produce levels having energies below the dashed line have been retained for the close-coupling expansion.

from the SUPERSTRUCTURE program (Eissner et al. 1974). AUTOSTRUCTURE constructs target wavefunctions using radial wavefunctions calculated in a scaled Thomas-Fermi-Dirac-Amaldi statistical model potential with a set of scaling parameters. The program also provides radiative rates and infinite energy Born limits. These limits are particularly important for two reasons. First, they allow a consistency check of the collision strengths in the scaled Burgess & Tully (1992) domain (see also Burgess et al. 1997). Second, they are used in the interpolation of the collision strengths at high energies.

The R-matrix method used in the scattering calculation is described in Hummer et al. (1993) and Berrington et al. (1995). We performed the calculation in the inner region in *LS* coupling and included mass and Darwin relativistic energy shifts.

The outer region calculation used the intermediate-coupling frame transformation (ICFT) method (Griffin et al. 1998), in which the transformation of the multi-channel quantum defect theory unphysical K-matrix to intermediate coupling uses the so-called term-coupling coefficients (TCCs) in conjunction with level energies.

Dipole-allowed transitions were topped-up to infinite partial wave using an intermediate coupling version of the Coulomb-Bethe method as described by Burgess (1974) while non-dipole allowed transitions were topped-up assuming that the collision strengths form a geometric progression in *J* (see Badnell & Griffin 2001).

The collision strengths were extended to high energies by interpolation using the appropriate high-energy limits in the Burgess & Tully (1992) scaled domain. The high-energy limits were calculated with AUTOSTRUCTURE for both optically-allowed (see Burgess et al. 1997) and non-dipole allowed transitions (see Chidichimo et al. 2003).

We have also carried out Breit-Pauli DW calculations using the recent development of the AUTOSTRUCTURE code, described in detail in Badnell (2011). We have used the same target for the DW and the ICFT calculations.

The temperature-dependent effective collisions strength $\Upsilon(i-j)$ were calculated by assuming a Maxwellian electron distribution and linear integration with the final energy of the colliding electron.

3. Results

Since we are primarily interested in the main diagnostics within the $n = 3$ levels, we have chosen a target which includes all the

Table 1. Target electron configuration basis and orbital scaling parameters λ_{nl} .

Configurations	Orbital	λ_{nl}
$3s^2 3p^6$	1s	1.41143
$3s^2 3p^5 3d$	2s	1.12797
$3s^2 3p^5 4l$ ($l = s, p, d, f$)	2p	1.06762
$3s^2 3p^4 3d^2$	3s	1.13741
$3s^2 3p^4 3d 4l$ ($l = s, p, d, f$)	3p	1.11363
$3s^2 3p^3 3d^3$	3d	1.11505
$3s 3p^4 3d^3$	4s	1.21162
$3p^5 3d^3$	4p	1.20995
$3s 3p^6 3d$	4d	1.19334
$3s 3p^6 4l$ ($l = s, p, d, f$)	4f	1.30588
$3s 3p^5 3d^2$		
$3s 3p^5 3d 4l$ ($l = s, p, d, f$)		
$3p^6 3d^2$		
$3p^6 3d 4l$ ($l = s, p, d, f$)		

main $n = 4$ levels. In our recent calculation for Fe IX (Del Zanna et al. 2014) we even included all the main $n = 5$ configurations, but for the $n = 3$ levels we did not find any significant differences in the collision strengths from the previous calculations (Storey et al. 2002), which included only $n = 3$ levels and the $3s^2 3p^5 4s$ and $3s^2 3p^5 4p$ configurations. This means that the $n = 5$ levels produce negligible resonance enhancement for the $n = 3$ levels. We also did not find significant differences for the $3s^2 3p^5 4s$ and $3s^2 3p^5 4p$ configurations, which again means that the $n = 5$ levels produce negligible resonance enhancement for these configurations.

We have therefore chosen as our configuration basis the complete set of 29 $n = 3, 4$ configurations, shown in Fig. 1 and listed in Table 1. They give rise to 1089 *LS* terms and 2635 fine-structure levels. The scaling parameters λ_{nl} for the potentials in which the orbital functions are calculated are also given in Table 1. The 599 fine-structure levels arising from the (energetically) lowest 273 *LS* terms were retained for the scattering calculation. They include all the spectroscopically important $n = 4$ levels.

Table 2 presents a selection of fine-structure target level energies E_t , compared to experimental energies E_{exp} . The experimental energies are mostly taken from the NIST compilation (Kramida et al. 2013), although we have revised some experimental energies (R in the Table) and suggested new tentative ones (TN in the Table), as described below in Sect. 3.1.

Table 2. Level energies for Ni XI.

<i>i</i>	Conf.	Mixing	Lev.	E_{exp}	E_t	
1	3s ² 3p ⁶	(96%)	¹ S ₀	0.0	0.0	
2	3s ² 3p ⁵ 3d	(96%)	³ P ₀	469 310.0	475 347.0 (−6037)	
3	3s ² 3p ⁵ 3d	(95%)	³ P ₁	472 970.0	479 422.0 (−6452)	
4	3s ² 3p ⁵ 3d	(93%)	³ P ₂	480 950.0	487 788.0 (−6838)	
5	3s ² 3p ⁵ 3d	(97%)	³ F ₄	493 250.0	502 075.0 (−8825)	
6	3s ² 3p ⁵ 3d	(88%)	³ F ₃	497 364.0	506 189.0 (−8825)	R
7	3s ² 3p ⁵ 3d	(84%)	³ F ₂	503 971.0	512 795.0 (−8824)	R
8	3s ² 3p ⁵ 3d	(63%) +12(33%)	³ D ₃	527 309.0	537 259.0 (−9950)	R
9	3s ² 3p ⁵ 3d	(56%) +7(11%) +11(28%)	¹ D ₂	530 687	540 935.0 (−10248)	R
10	3s ² 3p ⁵ 3d	(95%)	³ D ₁	534 830.0	544 664.0 (−9834)	
11	3s ² 3p ⁵ 3d	(60%) +9(32%)	³ D ₂	539 180.0	549 219.0 (−10039)	
12	3s ² 3p ⁵ 3d	(58%) +8(30%)	¹ F ₃	543 220.0	553 118.0 (−9898)	
13	3s ² 3p ⁵ 3d	(95%)	¹ P ₁	673 960.0	691 250.0 (−17290)	
14	3s3p ⁶ 3d	(77%) +121(c4 13%)	³ D ₁	–	859 654.0	
15	3s3p ⁶ 3d	(77%) +123(c4 13%)	³ D ₂	–	861 160.0	
16	3s3p ⁶ 3d	(78%) +118(c4 13%)	³ D ₃	839 979.0	863 728.0 (−23749)	TN
17	3s3p ⁶ 3d	(72%) +44(c4 14%)	¹ D ₂	–	889 505.0	
133	3s ² 3p ⁵ 4s	(61%) +139(36%)	³ P ₁	1 269 940.0	1 322 202.0 (−52262)	
139	3s ² 3p ⁵ 4s	(60%) +133(35%)	¹ P ₁	1 292 110.0	1 343 945.0 (−51835)	
335	3s ² 3p ⁵ 4d	(80%)	³ P ₁	1 571 310.0	1 615 059.0 (−43749)	
357	3s ² 3p ⁵ 4d	(68%) +385(27%)	¹ P ₁	1 594 130.0	1 628 741.0 (−34611)	?
440	3s3p ⁶ 4s	(70%) +972(c12 24%)	¹ S ₀	1 629 344.0	1 688 705.0 (−59361)	TN
525	3s ² 3p ⁵ 4f	(97%)	³ D ₁	1 701 800.0	1 762 546.0 (−60746)	
534	3s ² 3p ⁵ 4f	(91%)	³ D ₂	1 704 400.0	1 765 388.0 (−60988)	
540	3s ² 3p ⁵ 4f	(98%)	³ G ₅	1 706 600.0	1 768 505.0 (−61905)	
543	3s ² 3p ⁵ 4f	(78%) +588(10%)	³ D ₃	1 708 500.0	1 769 846.0 (−61346)	
545	3s ² 3p ⁵ 4f	(72%) +589(22%)	³ G ₄	1 709 045.0	1 771 320.0 (−62275)	R
553	3s ² 3p ⁵ 4f	(57%) +588(17%) +583(23%)	³ G ₃	1 714 400.0	1 776 707.0 (−62307)	
565	3s ² 3p ⁵ 4f	(48%) +589(44%)	³ F ₄	1 716 600.0	1 780 199.0 (−63599)	
583	3s ² 3p ⁵ 4f	(38%) +553(40%) +588(18%)	¹ F ₃	1 733 700.0	1 796 277.0 (−62577)	
588	3s ² 3p ⁵ 4f	(50%) +583(27%) +543(18%)	³ F ₃	1 736 100.0	1 798 185.0 (−62085)	
589	3s ² 3p ⁵ 4f	(30%) +545(20%) +565(46%)	¹ G ₄	1 736 600.0	1 798 761.0 (−62161)	
599	3s ² 3p ⁵ 4f	(64%) +577(26%)	¹ D ₂	1 739 500.0	1 808 761.0 (−69261)	

Notes. The first column indicates the (unique) level index, while the second the configuration. The third column indicates the mixing of the levels. For example, level No. 8 is a due by 63% to the ³D₃ and by 33% to the level No. 12, the ¹F₃. Only the main contributing terms (above 10%) are listed. The fourth column indicates the dominant *LSJ* contribution to the level. The experimental level energies E_{exp} (cm^{−1}) are shown in Col. 5 while Col. 6 lists those obtained from our scattering target E_t . Values in parentheses indicate differences between E_{exp} and E_t . Only a selection of levels is shown. R are revised values, TN tentative new ones.

A set of “best” energies E_b was obtained with a linear fit between the E_{exp} and E_t values. The E_b values were used (whenever the experimental energies E_{exp} were not available) within the R-matrix calculation to obtain a better position of the resonance thresholds. The experimental energies E_{exp} and the “best” energies E_b were also used to calculate the transition probabilities, which was done with a separate AUTOSTRUCTURE calculation.

The expansion of each scattered electron partial wave was done over a basis of 21 functions within the R-matrix boundary. The partial wave expansion within the exchange calculations was extended to a maximum total orbital angular momentum quantum number of $L = 16$. This produces reliable collision strengths up to about 70 Ryd.

The outer region calculation includes exchange up to a total angular momentum quantum number $J = 25/2$. We have added to the exchange contributions those from a non-exchange calculation, which extended from $J = 27/2$ to $J = 73/2$. The outer region exchange calculation was performed in a number of stages. A coarse energy mesh (with 96 points) was chosen above all resonances. The resonance region itself was calculated with an

increasing number of points, until 9600, so we could check the convergence, as in [Del Zanna et al. \(2010\)](#).

For diagnostic application purposes, it is useful to just discuss the atomic data for the strongest transitions. We have constructed an ion population model with the new R-matrix collision strengths, complemented with a set of A-values calculated separately with exactly the same configuration basis, but with the experimental and best energies. We then calculated line intensities and looked at how levels are populated at $\log N_e[\text{cm}^{-3}] = 9$ (a typical solar active region density) and $\log T_e[\text{K}] = 6.1$, the temperature of maximum ion abundance in ionization equilibrium. The brightest lines are listed in [Table 3](#). We also list, within the table, the intensities calculated with the CHIANTI model, which uses the [Aggarwal & Keenan \(2007\)](#) collision strengths for the first 17 levels and those of [Bhatia & Landi \(2011\)](#) for the rest. [Table 3](#) also lists our A-values, and those calculated by [Bhatia & Landi \(2011\)](#) with the FAC.

The intensities in the lines are relative to the strongest, resonance line (1–13, at 148.374 Å). The oscillator strength for this transition as calculated by [Aggarwal & Keenan \(2007\)](#) is 2.62 with FAC and 2.66 with GRASP, i.e. almost the same as our

Table 3. List of the strongest Ni XI lines.

$i-j$	Levels	I	I	gf	$A_{ji}(s^{-1})$	$A_{ji}(s^{-1})$	$\lambda_{exp}(\text{\AA})$	$\lambda_{th}(\text{\AA})$	
		CHIANTI		BL11					
1–13	$3s^23p^6\ ^1S_0-3s^23p^53d\ ^1P_1$	1.0	1.0	2.72	2.7×10^{11}	2.8×10^{11}	148.377	144.66	(–3.7)
5–95	$3s^23p^53d\ ^3F_4-3s^23p^43d^2\ ^3G_5$	5.1×10^{-2}	4.7×10^{-2}	5.12	1.2×10^{11}	1.3×10^{11}	–	152.54	
5–106	$3s^23p^53d\ ^3F_4-3s^23p^43d^2\ ^3D_3$	3.8×10^{-2}	3.7×10^{-2}	5.05	2.0×10^{11}	2.3×10^{11}	–	143.87	
5–114	$3s^23p^53d\ ^3F_4-3s^23p^43d^2\ ^3F_4$	3.5×10^{-2}	3.3×10^{-2}	5.92	2.0×10^{11}	2.2×10^{11}	–	137.72	
6–93	$3s^23p^53d\ ^3F_3-3s^23p^43d^2\ ^3G_4$	3.2×10^{-2}	2.9×10^{-2}	3.85	1.1×10^{11}	1.2×10^{11}	–	153.95	
6–107	$3s^23p^53d\ ^3F_3-3s^23p^43d^2\ ^3D_2$	1.9×10^{-2}	1.7×10^{-2}	3.30	1.9×10^{11}	2.1×10^{11}	–	144.40	
1–4	$3s^23p^6\ ^1S_0-3s^23p^53d\ ^3P_2$	0.19	0.12	–	1.4×10^2	1.4×10^2	207.922	205.01	(–2.9)
1–3	$3s^23p^6\ ^1S_0-3s^23p^53d\ ^3P_1$	9.1×10^{-2}	5.0×10^{-2}	3.8×10^{-4}	1.9×10^7	2.3×10^7	211.430	208.58	(–2.8)
1–10	$3s^23p^6\ ^1S_0-3s^23p^53d\ ^3D_1$	4.4×10^{-2}	2.3×10^{-2}	8.2×10^{-3}	5.1×10^8	5.7×10^8	186.975	183.60	(–3.4) (bl)
1–7	$3s^23p^6\ ^1S_0-3s^23p^53d\ ^3F_2$	2.2×10^{-2}	1.3×10^{-2}	–	5.9	5.6	198.42	195.01	(–3.4) R (bl)
1–9	$3s^23p^6\ ^1S_0-3s^23p^53d\ ^1D_2$	1.6×10^{-2}	9.6×10^{-3}	–	49.	51	188.435	184.87	(–3.6) R
5–16	$3s^23p^53d\ ^3F_4-3s3p^63d\ ^3D_3$	1.3×10^{-2}	2.0×10^{-2}	0.38	4.2×10^9	4.4×10^9	288.41	276.51	TN (bl)
1–139	$3s^23p^6\ ^1S_0-3s^23p^54s\ ^1P_1$	2.3×10^{-2}	4.9×10^{-3}	0.20	7.1×10^{10}	7.3×10^{10}	77.393	74.41	(–3.0)
1–133	$3s^23p^6\ ^1S_0-3s^23p^54s\ ^3P_1$	1.4×10^{-2}	4.1×10^{-3}	0.13	4.6×10^{10}	5.0×10^{10}	78.744	75.63	(–3.1) (bl)
13–440	$3s^23p^53d\ ^1P_1-3s3p^64s\ ^1S_0$	1.1×10^{-2}	5.6×10^{-3}	2.5×10^{-2}	1.5×10^{10}	7.9×10^9	104.67	100.25	TN
5–540	$3s^23p^53d\ ^3F_4-3s^23p^54f\ ^3G_5$	6.7×10^{-3}	5.5×10^{-3}	5.66	4.8×10^{11}	4.6×10^{11}	82.416	78.96	(–3.5)
13–599	$3s^23p^53d\ ^1P_1-3s^23p^54f\ ^1D_2$	5.5×10^{-3}	2.8×10^{-3}	1.93	3.4×10^{11}	2.0×10^{11}	93.849	89.49	(–4.4)
1–357	$3s^23p^6\ ^1S_0-3s^23p^54d\ ^1P_1$	4.0×10^{-3}	3.7×10^{-4}	0.58	3.1×10^{11}	7.7×10^{10}	62.730	61.40	(–1.3) ?
6–545	$3s^23p^53d\ ^3F_3-3s^23p^54f\ ^3G_4$	3.8×10^{-3}	2.9×10^{-3}	3.89	4.1×10^{11}	3.8×10^{11}	82.530	79.04	(–3.5)
5–187	$3s^23p^53d\ ^3F_4-3s^23p^54p\ ^3D_3$	3.5×10^{-3}	2.9×10^{-3}	0.30	2.2×10^{10}	2.2×10^{10}	–	106.60	
10–577	$3s^23p^53d\ ^3D_1-3s^23p^54f\ ^3F_2$	2.5×10^{-3}	2.5×10^{-3}	1.51	2.7×10^{11}	2.3×10^{11}	–	80.43	
6–186	$3s^23p^53d\ ^3F_3-3s^23p^54p\ ^3D_2$	2.4×10^{-3}	2.2×10^{-3}	0.17	1.8×10^{10}	1.8×10^{10}	–	107.49	
10–599	$3s^23p^53d\ ^3D_1-3s^23p^54f\ ^1D_2$	1.9×10^{-3}	1.3×10^{-3}	0.52	1.1×10^{11}	9.2×10^{10}	83.010	79.11	(–3.9)
5–12	$3s^23p^53d\ ^3F_4-3s^23p^53d\ ^1F_3$	6.7×10^{-2}	4.4×10^{-2}	–	2.7×10^2	2.8×10^2	2001.20	1959.12	(–42)
4–8	$3s^23p^53d\ ^3P_2-3s^23p^53d\ ^3D_3$	5.5×10^{-2}	3.8×10^{-2}	–	34	37	2157.08	2021.38	(–136) R
4–11	$3s^23p^53d\ ^3P_2-3s^23p^53d\ ^3D_2$	4.2×10^{-2}	2.6×10^{-2}	–	1.7×10^2	1.9×10^2	1717.33	1627.83	(–89.5)
6–8	$3s^23p^53d\ ^3F_3-3s^23p^53d\ ^3D_3$	3.1×10^{-2}	2.1×10^{-2}	–	19	21	3339.46	3218.54	(–121) R
6–9	$3s^23p^53d\ ^3F_3-3s^23p^53d\ ^1D_2$	2.9×10^{-2}	1.8×10^{-2}	–	86	95	3000.93	2878.03	(–123) R
7–9	$3s^23p^53d\ ^3F_2-3s^23p^53d\ ^1D_2$	1.8×10^{-2}	1.1×10^{-2}	–	54	59	3743.07	3553.69	(–189) R

Notes. The first column lists the indices of the levels, as from Table 2. The second the spectroscopic notation. Columns 3 and 4 show the intensities (photons) of the strongest lines, relative to the resonance transition, calculated at $\log N_e[\text{cm}^{-3}] = 9$ and $\log T_e[\text{K}] = 6.1$, using the present and the CHIANTI ion models. The CHIANTI model uses the Aggarwal & Keenan (2007) collision strengths for the first 17 levels and for the rest those of Bhatia & Landi (2011). Column 5 lists the weighted oscillator strength gf and Col. 6 the A-values from our calculation. Column 7 lists the Bhatia & Landi (2011) A-values as given in the CHIANTI v.7.1 database. TN is a tentative new identification, R a revised wavelength (compared to NIST), bl a blend. All wavelengths are in vacuum.

value (2.72), however, there is a considerable (about 30%) difference in the effective collision strength for this transition, as shown in Fig. 2. This difference results in a decrease of the predicted intensity of this line, hence affects all the ratios listed in Table 3. The reason for this difference is puzzling.

The oscillator strength for the resonance line as calculated with FAC by Bhatia & Landi (2011) is 2.67, i.e. it is also very close to ours. However, in that case their DW collision strengths are in good agreement with ours, as shown in Fig. 3. Our DW results are also in good agreement with the background collision strength as calculated with the R-matrix suite of codes, and the collision strength correctly converges toward the high-energy limit, so the effective collision strength for this line calculated by Aggarwal & Keenan (2007) is the odd one out.

A quick look at Table 3 clearly shows that many lines from the $3s^23p^53d$ levels are significantly increased in intensity, compared to the CHIANTI model. There is good agreement in the A-values, hence the differences are due to increased populations of the upper levels. For example, the populations of levels 3

and 4 are significantly increased. The reason is not just an increase in direct excitation to these levels, but a combined effect which includes increased cascading, in turn due the larger model and also increased excitation, similar to what we found for the coronal iron ions. Direct excitation contributes 25% to the population of level 3, while decays from levels 4 and 11 contribute 16%. The collision strengths to levels 3, 4, and 11 are all increased compared to the Aggarwal & Keenan (2007) results, as shown in Fig. 2. About 43% of the population of level 4 is due to decays from levels 8 and 11 and 15% to direct excitation from the ground state. Again, collision strengths to the 4, 8, and 11 levels are all increased compared to the Aggarwal & Keenan (2007) results.

On the other hand, there is good agreement with the CHIANTI model for the decays from the $3s^23p^43d^2$ levels, indicating that little resonance enhancement is present (at peak temperatures) in the present larger target, since in the CHIANTI model the excitation rates for these levels are derived from the DW collision strengths of Bhatia & Landi (2011).

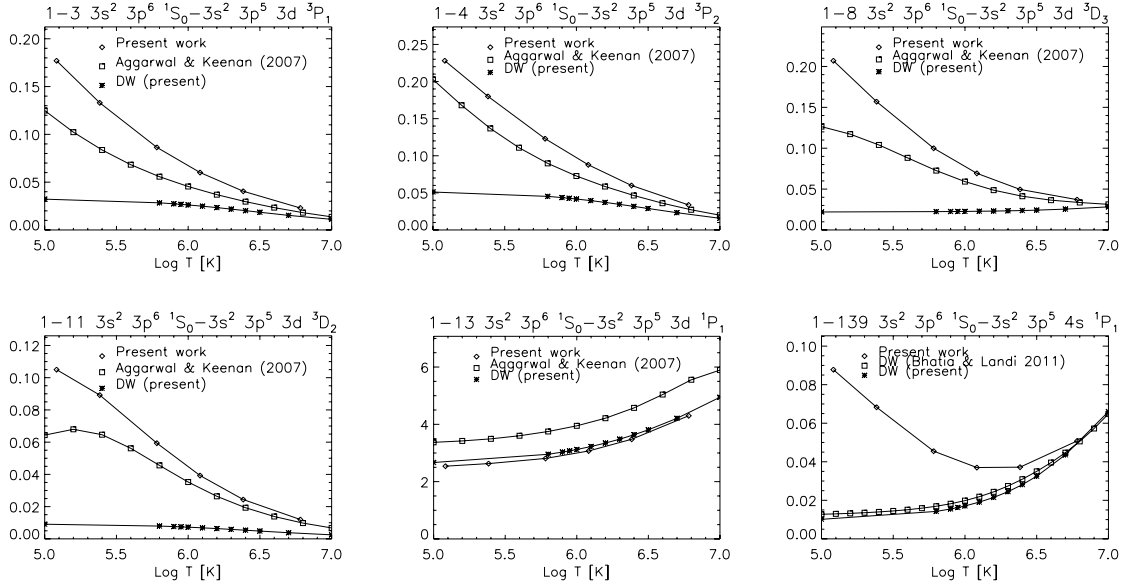


Fig. 2. Thermally-averaged collision strengths for a selection of transitions (see text).

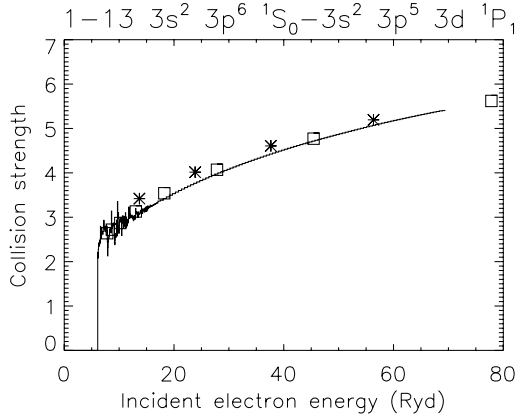


Fig. 3. Collision strength for the resonance 148.374 Å transition, averaged over 0.05 Rydbergs. Boxes: the results of our DW calculation. Stars: the results of the DW FAC calculation by [Bhatia & Landi \(2011\)](#).

Finally, for the $n = 3-4$ transitions, we find a similar situation as we saw for the iron coronal ions, i.e. significant increases in the intensities of many among the strongest transitions compared to the CHIANTI model. The A-values for the transitions generally agree well, so the main difference is due to the resonance enhancement that is present in the R-matrix calculations, but not in the DW values as calculated by [Bhatia & Landi \(2011\)](#) (note that our DW values are normally in good agreement with theirs). The effect is particularly pronounced for the $3s^2 3p^5 4s$ levels, where differences are factors of two or so. Figure 2 shows as an example the effective collision strength for the $3s^2 3p^6 1S_0-3s^2 3p^5 4s 1P_1$ transition, the strongest of the $n = 3-4$ array. Large enhancements also occur for the $3s^2 3p^5 4d$ levels.

3.1. Discussion on level identifications

The strongest resonance transition at 148.374 Å was identified by [Alexander et al. \(1965\)](#) which allowed the energy of the $3s^2 3p^5 3d^3 P_1$ level to be established. [Svensson et al. \(1974\)](#) applied some extrapolations along the isoelectronic sequence and used tentative identifications of some forbidden lines (at 3302.8,

3020.1, 2000.3, and 1715.3 Å) to suggest the identification of the three EUV solar lines observed by [Behring et al. \(1976\)](#) at 211.44, 207.935, and 186.983 Å with the decays from the $3s^2 3p^5 3d^3 P_2$, $3P_1$, and $3D_1$. These identifications, although tentative at the time, turned out to be important, because they allow the energies of these levels (relative to the ground state) to be established.

Surprisingly, [Edlen & Smitt \(1978\)](#) later revised some of the identifications of a few forbidden lines establishing the relative energies of some among the $3s^2 3p^5 3d$ levels. By combining these with the energies of the $3P_2$, $3P_1$, and $3D_1$ levels suggested by [Svensson et al. \(1974\)](#), it was therefore possible to establish also the energies of the $3F_4$, $3D_2$, and $1F_3$ levels. The energies of the other $3s^2 3p^5 3d$ levels were either estimated or known in terms of differences.

The main decays from the $3s^2 3p^5 4s$ and $3s^2 3p^5 4d$ configurations (from the $1P_1$ and $3P_1$) were identified using laboratory spectra by [Even-Zohar & Fraenkel \(1968\)](#). A few of the lines from the $3s^2 3p^5 3d-3s^2 3p^5 4f$ transition array were identified for the first time by [Fawcett et al. \(1972\)](#) using laboratory spectra. These lines were later re-measured by [Swartz et al. \(1976\)](#) with greater accuracy. With the measurements of the 81.378 and 81.138 Å lines, decays from the $3s^2 3p^5 4f^3 D_1$ (No. 525) to the $3s^2 3p^5 3d^3 P_{1,0}$ levels, we obtain the energy of the $3s^2 3p^5 3d^3 P_0$ level (No. 2).

We note that the energy of the $3s^2 3p^5 3d^3 F_2$ level adopted by NIST (504070 cm^{-1}) is the value suggested by [Edlen & Smitt \(1978\)](#), presumably based on the predicted energy difference with the known $3F_4$ level. This value turns out to be incorrect, because it predicts a wavelength of 198.38 Å for the decay to the ground state, which is not observed. Our theoretical splitting between the $3F_2$ and $3F_4$ levels suggests an energy of 503971 cm^{-1} for the $3F_2$, implying a wavelength of 198.42 Å for the decay to the ground state. There is indeed a weak line observed by Hinode EIS at exactly the right wavelength, at 198.424 Å ([Del Zanna 2012b](#)), and with about the right intensity.

Again using the theoretical $3F$ splittings, the estimated energy of the $3F_3$ should be 497364 cm^{-1} and not 497520 as listed by NIST. The energy of the $3D_3$ is only known relative to the $3F_3$ via the 3338.5 Å line (wavelength in air) as proposed

by [Edlen & Smitt \(1978\)](#), hence the energy of the 3D_3 should be $527\,309\text{ cm}^{-1}$ and not $527\,470\text{ cm}^{-1}$ as listed by NIST. The energy difference between this estimate and our target is 9950 cm^{-1} , in excellent agreement with the energy differences of the 3D_1 (9834 cm^{-1}) and 3D_2 ($10\,039\text{ cm}^{-1}$). A similar argument applies to the 1D_2 , for which we estimate the energy to be $530\,687$, and not $530\,830.0\text{ cm}^{-1}$ as listed by NIST. We obtain this number by adopting the observed wavelength (in air) of the $^3F_3-^1D_2$, 3000.0 \AA ([Edlen & Smitt 1978](#)), and our revised energy for the 3F_3 .

The energies of the $3s3p^63d$ levels are still unknown. [Landi & Young \(2009\)](#) proposed the identification of the $3s^23p^53d^3F_4-3s3p^63d^3D_3$ (5–16) transition with a line observed at 278.73 \AA , blended with Al V in their on-disk solar observation of a cool loop. The identification was presumably based on matching the ab-initio theoretical wavelength. We are unable to confirm this identification. If this line was partly due to Ni XI, it should be visible in off-limb spectra of the quiet Sun, where the Al V becomes invisible. In reality, there is no line in off-limb quiet-Sun spectra at this wavelength ([Del Zanna 2012b](#)). Also, the energy difference with our target energy would differ significantly from the energy differences of the other $3s^23p^53d$ levels. Applying the same energy difference of nearby levels results in a predicted wavelength of 288.5 \AA , very close to a line observed at 288.41 \AA , which is mostly due to S XII. It is interesting to note that [Behring et al. \(1976\)](#) indicate that in their high-resolution EUV spectrum the S XII line is blended with a first-order line. This line is therefore our best candidate for the 5–16 transition.

The main decays from the $3s^23p^54s$ configuration are the strongest Ni XI lines in the soft X-ray spectrum. One aspect which was puzzling at first is the fact that the line we predict to be strongest at 77.393 \AA was barely visible in the quiet Sun spectrum of [Behring et al. \(1972\)](#), and it is also weak in the [Manson \(1972\)](#) spectrum. The 78.744 \AA line should be much weaker but in the solar spectra it is much brighter. We thought at first that the identifications were incorrect but then checked the intensities of these lines against the resonance line, and found that the observed intensity of the 77.393 \AA is approximately in agreement with our predictions. This means that the 78.744 \AA line must be blended, and all the other Ni XI lines in the soft X-ray spectrum of the quiet Sun are extremely weak.

The third strongest line of the soft X-ray spectrum is the $3s^23p^53d^1P_1-3s3p^64s^1S_0$ (13–440) transition. We identified the same type of transitions (which are quite strong) for Fe X, Fe XI, Fe XII, and Fe XIII ([Del Zanna et al. 2012b](#); [Del Zanna 2012a](#)). Our “best” energy estimates predict this line to be around 104.6 \AA . There is indeed a weak line (on the blue-wing of another line) in the [Manson \(1972\)](#) and [Malinovsky & Heroux \(1973\)](#) spectra that we measured at 104.67 \AA , with the predicted intensity. We therefore suggest this as a tentative identification.

The strongest line from the $3s^23p^54p$ is predicted, again using the “best” energies E_b , to be around 112.6 \AA . There are two unidentified lines in the [Manson \(1972\)](#) and [Malinovsky & Heroux \(1973\)](#) spectra at 112.55 and 112.75 \AA , so it is possible that one of these is the 5–187 transition. Finally, we note that the energy of the $3s^23p^54d^1P_1$ level (No. 357) is at odds with the energy of the $3s^23p^54d^3P_1$, so the identification of the former is questionable.

3.2. Comparison to EUV observations

We now consider the main density diagnostic in the EUV for this ion, the 207.9 and 211.4 \AA lines. These lines are observed by

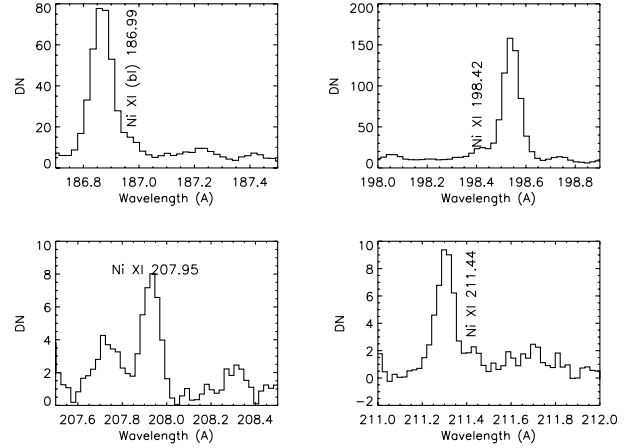


Fig. 4. A quiet Sun Hinode spectrum with the Ni XI lines.

Hinode EIS but they are at the very edge of one of the channels, where the instrument sensitivity is very low. In most Hinode EIS observations, these lines are not visible.

We have found an Hinode EIS full-spectral observation of the quiet Sun on 2010-10-08 at 10:15 UT, with the $2''$ slit and a very long exposure time (120 s), where these lines are visible. This observation was one of those selected for the radiometric calibration of the EIS instrument ([Del Zanna 2013](#)). We adopt this calibration here. We selected this observation because it provides typical quiet Sun line radiances. Despite this, the Ni XI lines are weak, as shown in Fig. 4 (units are recorded data numbers).

To compare the EIS radiances with that of the resonance line, we have taken the quiet Sun irradiance measured by the prototype EVE (PEVE) instrument ([Chamberlin et al. 2009](#); [Woods et al. 2009](#)) and converted into a radiance, assuming a limb-brightening factor of 1.4, as done in [Del Zanna \(2013\)](#), based on the limb-brightening curves obtained from SOHO CDS described in [Andretta & Del Zanna \(2014\)](#). Despite the uncertainty in the conversion, there is good agreement (within 20%) between predicted and observed radiances, as shown in Fig. 5. This figure shows the “emissivity ratio” curve

$$F_{ji} = \frac{I_{ob}N_e}{N_j(N_e, T_e) A_{ji}} C \quad (1)$$

for each line as a function of the electron density N_e . I_{ob} is the observed intensity of the line, $N_j(N_e, T_e)$ is the population of the upper level j relative to the total number density of the ion, calculated at a fixed temperature T_e . A_{ji} is the spontaneous radiative transition probability, and C is a scaling constant. This constant is the same for all the lines, and its value is 1.3×10^9 , for both plots in Fig. 5. This value was chosen so that the emissivity ratios are near unity, to visually estimate, from the spread in the curves, the relative agreement between observed and predicted intensities for all the lines. In fact, if agreement between experimental and theoretical intensities is present, all lines should be closely spaced. If the plasma is nearly isodensity, all curves should cross at one point, giving the line-of-sight averaged density. The emissivity ratio curves are useful to see at once the density sensitivity of the different emission lines, but are equivalent to the usual single line ratio plots, where the theoretical ratio of two emission lines is plotted as a function of density. The emissivity ratio curves in Fig. 5 are calculated at $\log T_e[\text{K}] = 6.1$, the temperature of maximum ion abundance in ionization equilibrium, i.e. the temperature where, in normal coronal conditions, the Ni XI lines are formed.

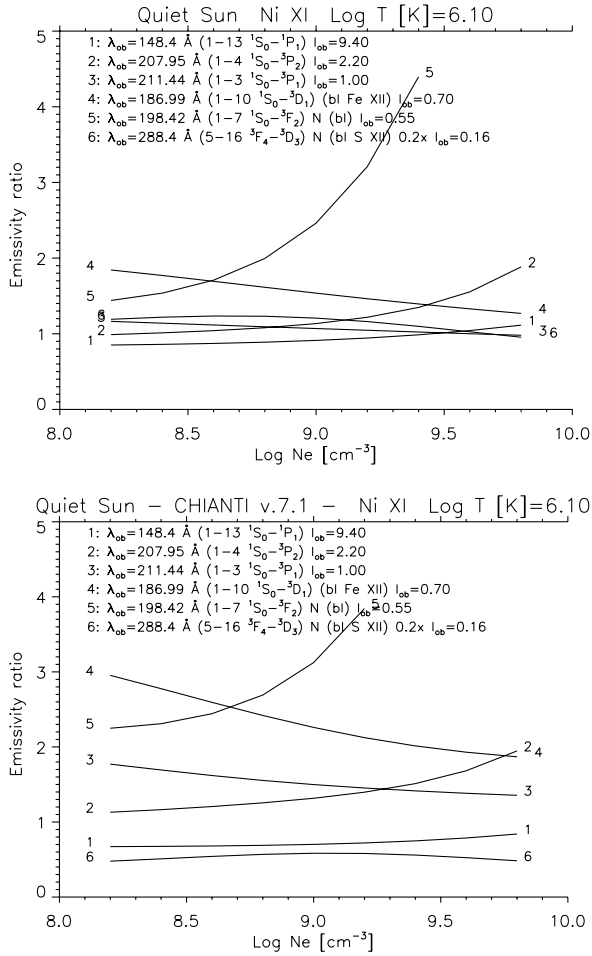


Fig. 5. Emissivity ratio curves relative to quiet Sun observations (Hinode EIS and PEVE, see text). *Above:* with the present atomic data. *Below:* with the AK07 atomic data as included in CHIANTI version 7.1. The observed intensities I_{ob} are in $\text{phot cm}^{-2} \text{s}^{-1} \text{arcsec}^{-2}$.

There is good agreement between predicted and observed intensities for all the lines, with the exception of the 198.42 Å very weak line, and the 186.99 Å line which is blended with an Fe XII transition. The emissivities of the 207.9 and 211.4 Å lines indicate that the electron density should be around $\log N_e[\text{cm}^{-3}] = 8.8$, although the observation is consistent with any lower density, considering the large uncertainty in the measurement of the weaker 211.4 Å line (say 30%), and the overall uncertainty in the relative Hinode EIS calibration between the two lines (typical uncertainties are 10–20%, see Del Zanna 2013). On the other hand, the CHIANTI v.7.1 model indicates an unreasonably high density of $\log N_e[\text{cm}^{-3}] = 9.3$, and a large discrepancy between the quiet Sun radiance of the resonance line and the well-measured 207.9 Å line.

4. Conclusions

The present scattering calculations produced the expected results, i.e. enhanced collision strengths for transitions to the $3s^23p^53d$ and $n = 4$ levels (in particular the $3s^23p^54s$), compared to the previous R-matrix and DW results of Aggarwal & Keenan (2007) and Bhatia & Landi (2011). The increases are due to the resonances that arise within the present large-scale target.

This results in significant increases in the predicted intensities of the UV and visible forbidden lines within the $3s^23p^53d$ configuration, the strong EUV lines that result from the decays of the $3s^23p^53d$ levels to the $3s^23p^61S_0$ ground state and the decays from the $n = 4$ levels, which are visible in the soft X-rays.

The present atomic dataset can now reliably be used for plasma diagnostics. We had a close look at the experimental energies and found the need for some revisions. Further laboratory work is needed to confirm some of the suggested new identifications, and complete the identification of the main levels for this ion.

Acknowledgements. The present work was funded by STFC (UK) through the University of Cambridge DAMTP astrophysics grant, and the University of Strathclyde UK APAP network grant ST/J000892/1.

References

- Aggarwal, K. M., & Keenan, F. P. 2007, *A&A*, 475, 393
 Alexander, E., Feldman, U., & Fraenkel, B. S. 1965, *J. Opt. Soc. Am.*, 55, 650
 Andretta, V., & Del Zanna, G. 2014, *A&A*, 563, A26
 Badnell, N. R. 2011, *Comput. Phys. Comm.*, 182, 1528
 Badnell, N. R., & Griffin, D. C. 2001, *J. Phys. B Atom. Mol. Phys.*, 34, 681
 Behring, W. E., Cohen, L., & Feldman, U. 1972, *ApJ*, 175, 493
 Behring, W. E., Cohen, L., Doschek, G. A., & Feldman, U. 1976, *ApJ*, 203, 521
 Berrington, K. A., Eissner, W. B., & Norrington, P. H. 1995, *Comput. Phys. Comm.*, 92, 290
 Bhatia, A. K., & Landi, E. 2011, *Atom. Data Nucl. Data Tables*, 97, 50
 Burgess, A. 1974, *J. Phys. B Atom. Mol. Phys.*, 7, L364
 Burgess, A., & Tully, J. A. 1992, *A&A*, 254, 436
 Burgess, A., Chidichimo, M. C., & Tully, J. A. 1997, *J. Phys. B Atom. Mol. Phys.*, 30, 33
 Chamberlin, P. C., Woods, T. N., Crotsler, D. A., et al. 2009, *Geophys. Res. Lett.*, 36, 5102
 Chidichimo, M. C., Badnell, N. R., & Tully, J. A. 2003, *A&A*, 401, 1177
 Culhane, J. L., Harra, L. K., James, A. M., et al. 2007, *Sol. Phys.*, 60
 Del Zanna, G. 2012a, *A&A*, 546, A97
 Del Zanna, G. 2012b, *A&A*, 537, A38
 Del Zanna, G. 2013, *A&A*, 555, A47
 Del Zanna, G., & Storey, P. J. 2013, *A&A*, 549, A42
 Del Zanna, G., Storey, P. J., & Mason, H. E. 2010, *A&A*, 514, A40
 Del Zanna, G., Storey, P. J., Badnell, N. R., & Mason, H. E. 2012a, *A&A*, 543, A139
 Del Zanna, G., Storey, P. J., Badnell, N. R., & Mason, H. E. 2012b, *A&A*, 541, A90
 Del Zanna, G., Storey, P. J., Badnell, N. R., & Mason, H. E. 2014, *A&A*, 565, A77
 Edlen, B., & Smitt, R. 1978, *Sol. Phys.*, 57, 329
 Eissner, W., Jones, M., & Nussbaumer, H. 1974, *Comput. Phys. Comm.*, 8, 270
 Even-Zohar, M., & Fraenkel, J. 1968, *J. Opt. Soc. Am.*, 58, 1420
 Fawcett, B. C., Kononov, E. Y., Hayes, R. W., & Cowan, R. D. 1972, *J. Phys. B Atom. Mol. Phys.*, 5, 1255
 Griffin, D. C., Badnell, N. R., & Pindzola, M. S. 1998, *J. Phys. B Atom. Mol. Phys.*, 31, 3713
 Gu, M. F. 2004, in *AIP Conf. Ser.* 730, eds. J. S. Cohen, D. P. Kilcrease, & S. Mazavet, 127
 Hummer, D. G., Berrington, K. A., Eissner, W., et al. 1993, *A&A*, 279, 298
 Kramida, A., Ralchenko, Yu., Reader, J., & NIST ASD Team 2013, *NIST Atomic Spectra Database*, v. 5.1. <http://physics.nist.gov/asd>
 Landi, E., & Young, P. R. 2009, *ApJ*, 706, 1
 Malinovsky, L., & Heroux, M. 1973, *ApJ*, 181, 1009
 Manson, J. E. 1972, *Sol. Phys.*, 27, 107
 Mattioli, M., Fournier, K. B., Coffey, I., et al. 2004, *J. Phys. B Atom. Mol. Phys.*, 37, 13
 O'Dwyer, B., Del Zanna, G., Badnell, N. R., Mason, H. E., & Storey, P. J. 2012, *A&A*, 537, A22
 Storey, P. J., Zeippen, C. J., & Le Dourneuf, M. 2002, *A&A*, 394, 753
 Svensson, L. Å., Ekberg, J. O., & Edlén, B. 1974, *Sol. Phys.*, 34, 173
 Swartz, M., Kastner, S. O., Goldsmith, L., & Neupert, W. M. 1976, *J. Opt. Soc. Am.* (1917–1983), 66, 240
 Woods, T. N., Chamberlin, P. C., Harder, J. W., et al. 2009, *Geophys. Res. Lett.*, 36, 1101